Journal of Materials Chemistry A

Stanene Nanomesh as Anode Material for Na-ion Batteries

Journal:	*Journal of Materials Chemistry A*
Manuscript ID	TA-ART-02-2018-001716.R1
Article Type:	Paper
Date Submitted by the Author:	28-Mar-2018
Complete List of Authors:	Wu, Liyuan; State Key Laboratory of Information Photonics and Optical Communications,Ministry of Education, Beijing University of Posts and Telecommunications Lu, Pengfei; State Key Laboratory of Information Photonics and Optical Communications,Ministry of Education, Beijing University of Posts and Telecommunications Quhe, Ruge; Beijing University of Posts and Telecommunications, wang, qian; Beijing University of Posts and Telecommunications, Yang, Chuanghua; Shanxi University of Technology, Guan, Pengfei; CSRC Yang, Kesong; University of California, San Diego, NanoEngineering Department

Journal Name

ARTICLE TYPE

Cite this: DOI: 10.1039/xxxxxxxxxx

Stanene Nanomesh as Anode Material for Na-ion Batteries†

Liyuan Wu,[a,b] Pengfei Lu,[a,c*] Ruge Quhe,[a,d] Qian Wang,[a] Chuanghua Yang,[e] Pengfei Guan,[f] and Kesong Yang[b*]

Received Date
Accepted Date

DOI: 10.1039/xxxxxxxxxx

www.rsc.org/journalname

Two-dimensional (2D) materials are showing promising potential in the energy storage applications such as being as electrodes of metal-ion batteries. Here, we explore the possibility of 2D stanene as anode material in the Na-ion battery using first-principles calculations, and particularly elucidate the role of a nanomesh structure in improving the battery performance. Our results show that the 2D stanene tends to form nanohole defects that consist of six Sn vacancies in a hexagonal ring, and the hydrogen passivation on the edge of the nanohole can further lower the formation energy. On the basis of this finding, we model nanohole-patterned stanene nanomesh (SnNM) structure and evaluate its performance as an anode material in the Na-ion battery. It is found that the nanohole defects in the 2D stanene can increase Na binding intensity and lower Na diffusion energy barrier as low as 0.15 eV. A denser SnNM is expected to further improve battery performance because of larger capacity, lower Na diffusion energy barrier, and resulting faster charge-discharge rate. This work shows that a nanomesh structure in the 2D material is beneficial to enhance the performance of metal-ion battery.

1 INTRODUCTION

Sodium-ion batteries (NIBs) have attracted increasing interests as promising alternatives for lithium-ion batteries because of their low cost and the earth abundance of sodium (Na).[1–3] However, the development of electrode materials, especially anode materials, for NIBs is still a challenge. This is because Na has a larger ionic radius than Li and thus its diffusion rate is generally slow with respect to Li, which make it hard to incorporate with the commercial anode materials such as graphite.[4–6] Therefore, it is necessary to search for safe, abundant, and robust materials for NIB anodes. As a promising class of anode materials, two-dimensional (2D) materials have attracted wide attention because their unique layered morphology enables large-area metal-ions adsorption and fast ion diffusion.[7–9] For instance, 2D layered MoS_2 has been explored as one anode material for NIBs, with a maximum theoretical capacity of 146 mAh/g and a diffusion barrier of 0.28 (0.68) eV for 1T (2H) phase of MoS_2.[10] By using phosphorene as an anode for NIBs, Kulish *et al*.[11] has achieved a theoretical capacity of 865 and 433 mAh/g for the NIBs with double- and single-side Na adsorption models, respectively. Besides, several other 2D materials such as phosphorene-like SiS and SiSe,[12] Ca_2N,[13] and silicene[14] have also been widely studied as possible anode materials for NIBs.

Atomic defects such as vacancies often exist in 2D materials,[15] and these vacancy defects can form porous or nanomesh structures.[16,17] One feature of porous or/and nanomesh structures is to enhance functionalities of 2D materials in practical applications such as field-effect transistors,[16,18] gas sensors or biosensors,[19,20] and energy storage including gas storage,[21] supercapacitors,[22] and lithium-ion batteries (LIBs).[23] As for LIBs, one advantage of porous or/and nanomesh structure is to improve the capacity and performance of LIBs. For instance, Fan *et al*. reported that porous graphene can not only provide more edges for enhancing Li^+ storage and thus improve the reversible capacity to 1723 mAh/g but also reduce diffusion resistance and diffusion distance.[24] In a later experimental study, Ren *et al*.[25] introduced pores into 2D transition metal carbide (MXene) $Ti_3C_2T_x$ using a chemical etching method, and reported that the porous $Ti_3C_2T_x$ films have a much higher Li ion storage capability of LIBs with respect to pristine $Ti_3C_2T_x$ based films, with a high capacity 1250

[a] State Key Laboratory of Information Photonics and Optical Communications, Beijing University of Posts and Telecommunications, Beijing 100876, China
[b] Department of NanoEngineering, University of California San Diego, 9500 Gilman Drive, Mail Code 0448, La Jolla, California 92093-0448, USA
[c] State Key Laboratory of Functional Materials for Informatics, Shanghai Institute of Microsystem and Information Technology, Chinese Academy of Sciences, Shanghai 200050, China
[d] School of Science, Beijing University of Posts and Telecommunications, Beijing 100876, China
[e] School of Physics and Telecommunication Engineering, Shaanxi University of Technology(SNUT), Hanzhong 723001, Shaanxi, China
[f] Beijing Computational Science Research Center, Beijing 100084, China
* Corresponding atuhor; E-mail: photon.bupt@gmail.com, kesong@ucsd.edu

mAh/g, excellent cycling stability, and good rate performance. On the basis of these findings, one may speculate the porous or nanomesh structures of the 2D materials can also be effective to improve performance of NIBs.

Recently, stanene, a single layer structure consisting of Sn atoms in a manner like graphene, has drawn particular interests due to its exceptional electronic properties, such as quantum spin Hall state,[26] enhanced thermoelectricity,[27] topological superconductivity,[28,29] and the near-room-quantum anomalous Hall effect.[30] Moreover, stanene can be fabricated either as a free-standing structure[31] or on a substrate,[32] which further promotes computational studies of strain effects on the mechanical, electronic, and optical properties of stanene.[33–35] Since stanene shares a similar layer structure with the graphene, one may hypothesize that 2D stanene can also serve as an anode material for metal-ion batteries.[36] Actually, bulk Sn metal as anode material has been explored in a recent experiment though it suffers from poor cycling stability.[37] However, the stanene nanomesh (SnNM) structure has not been investigated as anode material for NIBs.

In this work, by using first-principles calculations, we explored the possibility of 2D stanene and SnNM as anode materials in the NIBs and studied the influence of patterned nanoholes on the Na binding energy, Na adsorption intensity, and Na diffusion energy barrier. Our calculations indicate that a nanomesh structure in the 2D stanene can enhance the performance of NIBs by increasing Na adsorption intensity and decreasing Na diffusion energy barrier. We organize this article as below. First, we studied the formation of nanohole in stanene, which results from the reconstruction of vacancies. Then, we investigated the behaviors of Na adsorption on pristine stanene, stanene with nonohole and SnNM. At last, we evaluated the performance of SnNM as an anode material for NIBs in the aspects of open-circuit voltage, theoretical capacity and Na diffusion process.

2 COMPUTATIONAL DETAILS

Our first-principles calculations were performed using Vienna Ab initio Simulation Package (VASP).[38] The projected augmented wave (PAW) potentials were used to treat the interactions between core electrons and valence electrons.[39] The electron exchange-correlation functional was described by the Perdew-Burke-Ernzerhof (PBE) within the generalized gradient approximation (GGA).[40] The c-parameter of each unit cell along the z-direction was maintained at 20 Å to eliminate the interaction between periodic images of slabs. The plane-wave energy cutoff was set to be 300 eV. The convergence criterion for a total energy was set as 10^{-5} eV. All the atomic positions and lattice structures were fully relaxed with the threshold of a maximum force of 10^{-2} eV/Å. The Gamma-centered k-points mesh with Monkhorst-Pack scheme from $11\times11\times1$ to $5\times5\times1$ was employed,[41] with a k-point separation smaller than 0.01 $Å^{-1}$ in the Brillouin zone for all considered models. The amount of charge transfer between Na atom and stanene nanomesh was calculated using Bader code.[42]

To study Na diffusion kinetics, we calculated Na diffusion energy barriers using climbing image nudged elastic band (CI-NEB) method.[43] The CI-NEB is an efficient method to determine the minimum energy path and saddle points between a given initial and final position.[44,45] In our CI-NEB calculations, the start and end points of the structures were fully optimized, and three intermediate images were linearly interpolated. The lowest energy configuration was searched along the reaction path based on each image. The CI-NEB calculations were performed with $10\times10\times1$, $6\times6\times1$ and $5\times5\times1$ Monkhorst-Pack k-points meshes and a convergence criterion of 10^{-2} eV/Å in force.

3 RESULTS AND DISCUSSION

3.1 Structural Reconstruction of Vacancies

Vacancy defects often exist in the two-dimensional materials such as graphene and silicene.[46,47] Here we started by studying structural reconstruction of vacancies in the monolayer stanene. The vacancy defects are built by removing n (n = 1-6) Sn atoms from a hexagonal ring in a 96-atom rectangular supercell. For convenience, these defected structures with Sn vacancies are defined as V_{Snn}. For example, at n = 6, a hexagonal nanohole will be formed. The relaxed structures are shown in Fig. 1. The calculated lattice parameters, deformation parameters, and formation energies are shown in Table 1. For the pristine stanene, the lattice constants are $a_0 = 32.325$ Å and $b_0 = 28.080$ Å. For stanene with Sn vacancy defects, after structural relaxation, the lattice constants of the supercell decrease, leading to a compressive deformation along the armchair and zigzag directions. To evaluate deformation degree of stanene, we defined deformation parameters along armchair and zigzag directions using the equations: $\Delta a = (a - a_0)/a_0$ and $\Delta b = (b - b_0)/b_0$, respectively, in which a_0 and b_0 are the lattice constants of pristine stanene. Our results show that V_{Sn6} has the most uniform structure with the smallest deformation among all the defected structures. V_{Sn6} is also most similar to pristine stanene, as shown from their side views in Fig. 1a' and 1g'. At n=1, one single Sn vacancy can cause a distortion of stanene's hexagonal arrangement as show in Fig. 1(b). At n>2, after relaxation, there is a significant structural reconstruction around the vacancy, forming a nanohole. For example, V_{Sn2} becomes an eight-member (oval-shape) hole surrounded by two pentagons and six hexagons and V_{Sn3} becomes a ten-membered (heart-shape) hole surrounded by two pentagons and seven hexagons. For these reconstructed nanoholes, we use maximum diameter (D) of the circle in the hole region to evaluate the size of these holes, see the black arrow in Fig. 1(c-h). It clearly shows that V_{Sn6} has a larger hole size than all other defected structures.

To compare relative stability of stanene with different numbers of vacancies, we calculated the formation energies per atom using the equation,

$$E_f = \frac{E_{V_{Snn}} - E_{\text{pristine}} + nE_{\text{Sn}}}{n} \quad (1)$$

where $E_{V_{Snn}}$ and E_{pristine} are the total energies of V_{Snn} and pristine stanene, respectively. E_{Sn} is the average energy per Sn atom of the pristine stanene and n is the number of removed Sn atoms. The calculated formation energies are summarized in Table 1. Our results show that V_{Sn1} has the largest formation energy mainly because of a large distortion of stanene's hexagonal reconstruction. All other defected structures from V_{Sn2} to V_{Sn6} have relative small formation energies. This is because they are all recon-

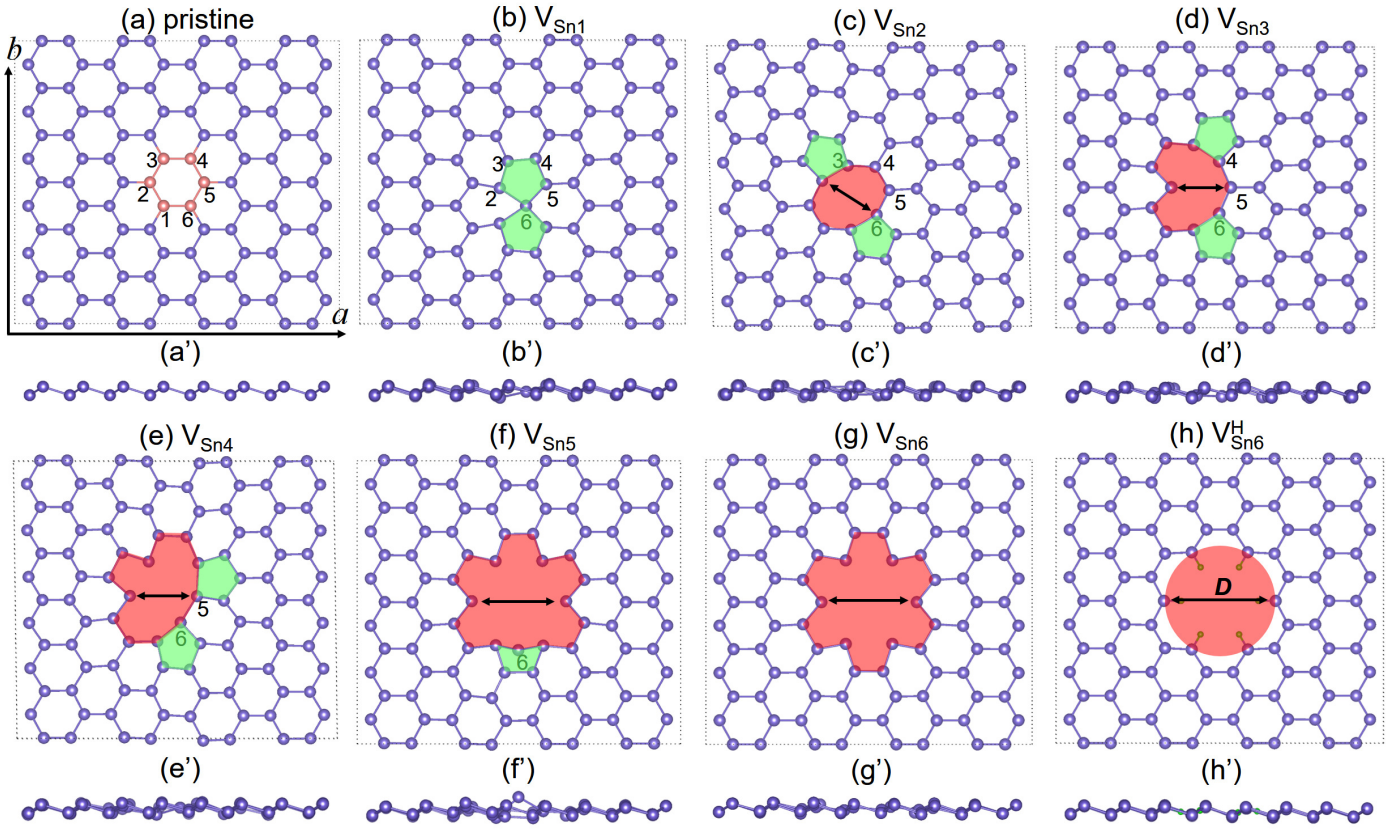

Fig. 1 Schematic of fully relaxed stanene structures. (a) Pristine stanene, (b-g) stanene with n vacancies (labeled as $V_{Sn}$$_n$, n = 1-6), and (h) stanene with hydrogen passivated V_{Sn6} defect (labeled as V^{H}_{Sn6}). The corresponding side views are shown as (a'-h'). The six Sn atoms to be removed are numbered as 1-6 shown in (a). The nanoholes formed from the reconstruction of vacancies are highlighted as red zones and the black arrows in (c-h) show the diameter of the nanoholes.

structed to form a nanohole structure as shown in Fig. 1(c-g). It is worth pointing out that V_{Sn5} and V_{Sn6} have similar structures and thus comparable formation energies. Their difference is that in the V_{Sn5} some Sn atoms around the hole protrude out from the plane, which leads to a structural distortion, see its side view in Fig. 1f'. In general, V_{Sn6} has the smallest deformation and lowest formation energy, and thus can be easily formed in stanene. This finding is well consistent with the case in the graphene in which similar hexagonal nanoholes are formed and observed.[16]

It is widely known that dangling bonds of atoms on the hole edge are chemically active,[32] and the hole edge would often be passivated by functional group such as hydrogen. For instance, it has been proved that hydrogen can stabilize nanoholes in graphene by passivating dangling bonds at the hole rim,[48] and C-H bonds at graphene defects were observed experimentally using muon spectroscopy.[49] As a result, one might speculate that a similar passivation by hydrogen may also occur in the defected stanene structure. To further study possible passivation of V_{Sn6} structure, we used hydrogen to passivate the Sn atoms at the hole edge of V_{Sn6} and calculated its formation energy. This hydrogen-passivated structure was labeled as V^{H}_{Sn6}, see Fig. 1h. Its relaxed structure is almost unchanged compared to the pristine stanene from side views (Fig. 1a' and 1h'). Its hole diameter is up to 11.10 Å, much close to that of the unrelaxed structure. Its lattice deformation is also much smaller than all other unpassivated defected structures, see Table 1. The corresponding formation energy of V^{H}_{Sn6} is calculated using the equation $E_f = (E_{V_{Sn6}} - E_{pristine} + 6E_{Sn} - 6\mu_H)/6$, where μ_H is taken from the total energy of H_2 molecule. Our calculations show that the formation energy of V^{H}_{Sn6} significantly decreased compared to that unpassivated V_{Sn6} structure (0.44 *versus* 0.68 eV/Sn). All these results indicate that V^{H}_{Sn6} is energetically most favorable among all the considered structures.

3.2 Na Adsorption on Stanene

In this section, we calculated the binding energy (E_b) of Na adsorbed stanene using the equation,

$$E_b = (E_{stanene} + mE_{Na} - E_{Na@stanene})/m \quad (2)$$

where $E_{stanene}$ is the energy of stanene, E_{Na} is the energy of an isolated Na atom, $E_{Na@stanene}$ is the total energy of Na adsorbed stanene and m is the number of adsorbed Na atoms. Note that the binding energy is sensitive to Na adsorption sites. In the pristine stanene, there are three possible adsorption sites even for a single Na atom adsorption: hollow (H) site above the center of a hexagon, top (T) site of Sn atoms, bridge (B) site of Sn-Sn atoms, see Fig. 2a. The binding energies at these sites are summarized in Table 2. A larger binding energy at one site means that the Na

Table 1 Geometric and energetic parameters of the relaxed pristine stanene, V_{Snn} and V^{H}_{Sn6}, including lattice constants (a and b), deformation parameter along armchair and zigzag directions (Δa and Δb), diameter of the hole size (D) and formation energy per removed Sn atom (E_f).

Structure	a (Å)	b (Å)	Δa (%)	Δb (%)	D (Å)	E_f(eV/Sn)
pristine	32.325	28.080	0	0	-	-
V_{Sn1}	32.050	27.884	-0.85	-0.70	-	1.86
V_{Sn2}	31.856	28.042	-1.45	-0.13	6.47	0.69
V_{Sn3}	31.745	27.956	-1.79	-0.44	5.92	0.74
V_{Sn4}	32.021	27.713	-0.94	-1.30	6.70	0.81
V_{Sn5}	32.048	27.986	-0.86	-0.33	9.41	0.67
V_{Sn6}	32.142	27.977	-0.57	-0.36	9.42	0.68
V^{H}_{Sn6}	32.328	28.057	0.008	-0.08	11.10	0.44

atom tends to be adsorbed at this site via a strong bonding interaction. For the pristine stanene, H site has a maximum binding energy of 1.82 eV, indicating that H site is the most possible one to absorb Na ions. When Na is absorbed at H site, the bonding distance (d) of Na with the nearest Sn atom is 3.22 Å, and the height (h) between Na and stanene plane is 2 Å. For structure V^{H}_{Sn6}, besides the H site, T site, and B site, we also modeled edge (E) hollow sites and center (C) site of the nanohole, see Fig. 2(b). Note that based on the distance between the adsorption site and the nanohole, we considered two H sites. The calculated results show that the binding energies at H sites are quite close to that in the pristine stanene, indicating the nanohole has little effect on the H site. The E site of V^{H}_{Sn6} has a maximum binding energy about 2.11 eV, and thus it is the most possible site to absorb Na ions. When absorbed at E site, the Na ion is located in the plane of stanene with d = 3.33 Å and h = 0 Å. These results reveal that the hydrogenated nanohole can enhance the binding intensity between Na ion and stanene, especially for the Na ions in the nanohole.

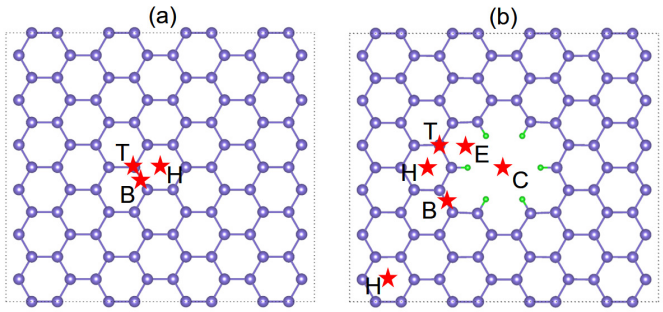

Fig. 2 Schematic of possible Na adsorption sites on (a) pristine stanene and (b) V^{H}_{Sn6}. The adsorption sites are marked by red stars: hollow (H) site above the center of hexagon, top (T) site of Sn atom, bridge (B) site of Sn-Sn atoms, edge (E) hollow site, and center (C) site of nanohole.

In addition, to study the binding interaction between the Na atom and stanene, we calculated the electron charge density differences for pristine stanene with Na adsorbed at H site and V^{H}_{Sn6} with Na adsorbed at H site and E site (see Fig. 3). The red and green colors represent charge accumulation and reduction, respectively. It shows that the electrons accumulate around Sn atoms and decrease around the Na atom, indicating a charge transfer from Na to stanene. The charge transfer is also confirmed by using Bader charges analysis. Our calculations show that there is a charge transfer of 0.763, 0.637, and 0.665 electrons to stanene for pristine stanene with Na adsorbed at H site and V^{H}_{Sn6} with Na adsorbed at H and E site, respectively.

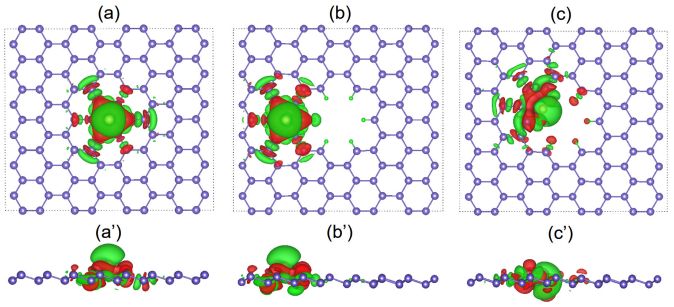

Fig. 3 Top views of electron charge density difference for (a) pristine stanene with Na adsorbed at H site and V^{H}_{Sn6} with Na adsorbed at (b) H site and (c) E site. The corresponding side views are shown as (a'-c'). The isosurface level is 0.0002 e/Bohr^3. The red and green colors represent charge accumulation and reduction, respectively.

Table 2 Binding energies E_b (eV) of pristine stanene, V^{H}_{Sn6}, and SnNMs with Na adsorbed at different sites. "to H or E" represents that Na atom moves to H or E site after full relaxation.

Sites	pristine	V^{H}_{Sn6}	SnNM		
			W=2	W=3	W=4
H	1.82	1.84(1.80[1])	1.71	1.90	1.83
T	1.63	1.83(to H)	1.53	1.68	1.72
B	1.63	1.68	1.64	1.68	1.72
E	-	2.11	2.06	2.19	2.15
C	-	2.12(to E)	1.07	1.20	2.14(to E)

[1] This value is obtained from the hollow site far away from the nanohole.

3.3 Na Adsorption on Stanene Nanomesh

As discussed above, V^{H}_{Sn6} has the smallest formation energy and thus can be easily formed. Actually, such a nanohole structure has been experimentally observed in the graphene and these nanoholes tend to be formed periodically.[16,50] The two-dimensional layer structure with patterned nanoholes is also known as nanomesh.

Next, we explored the Na adsorption on SnNM structures. In this work, SnNM is built by constructing periodic hexagonal

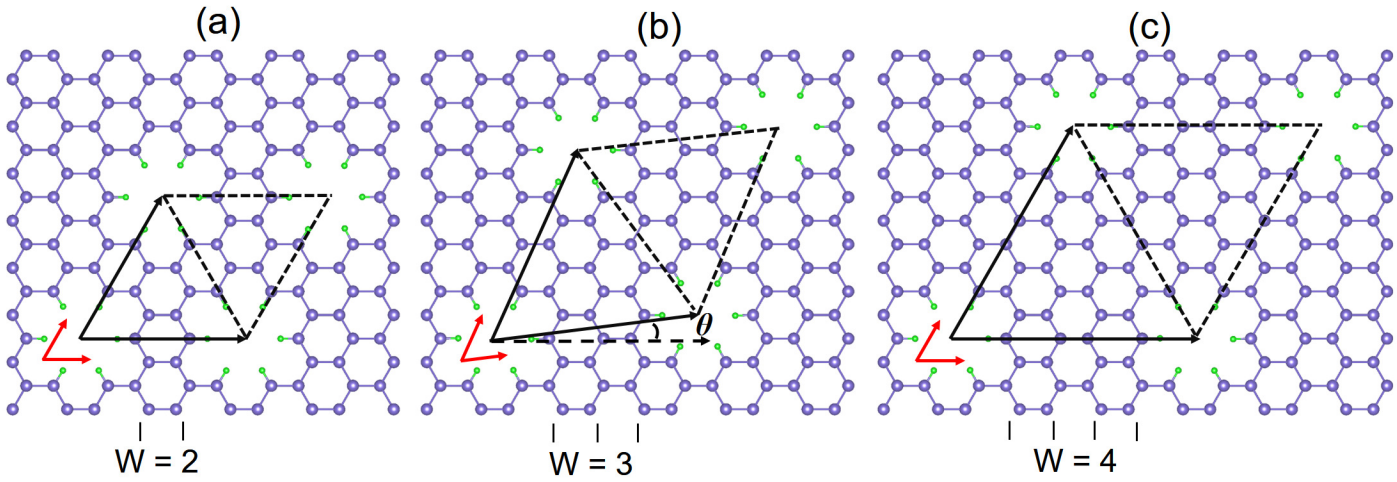

Fig. 4 Geometric configurations of three types of stanene nanomesh (SnNM): (a) W=2, (b) W=3, and (c) W=4. W is the width of the stanene chain along zigzag direction between the neighboring holes. The three configurations represent the nanohole density of $4.44\times10^{13}\,cm^{-2}$, $2.79\times10^{13}\,cm^{-2}$, and $1.97\times10^{13}\,cm^{-2}$, respectively. The lattice vectors for the unit cells are indicated by the red arrow lines. The two lattice vectors are along the armchair directions for the structures with even W=2 and 4, and along the chiral directions with a tilted angle $\theta = tan^{-1}\frac{\sqrt{3}}{3(W+2)}$ deviating from the armchair directions for the structure with an odd W=3. θ = 6.6° at W=3.

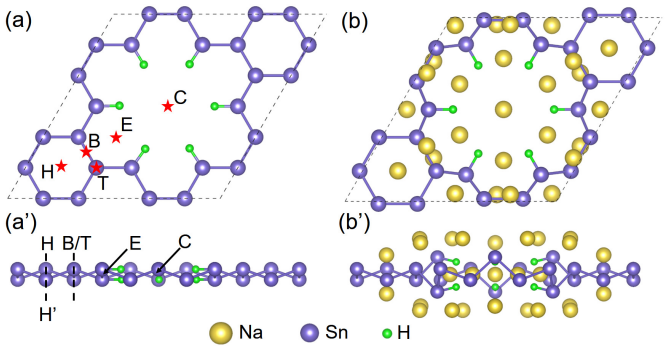

Fig. 5 (a) Top and (a') side views of five possible Na adsorption sites on the SnNM with W=2. (b) Top and (b') side views of optimized structure of Na fully adsorbed SnNM with W=2.

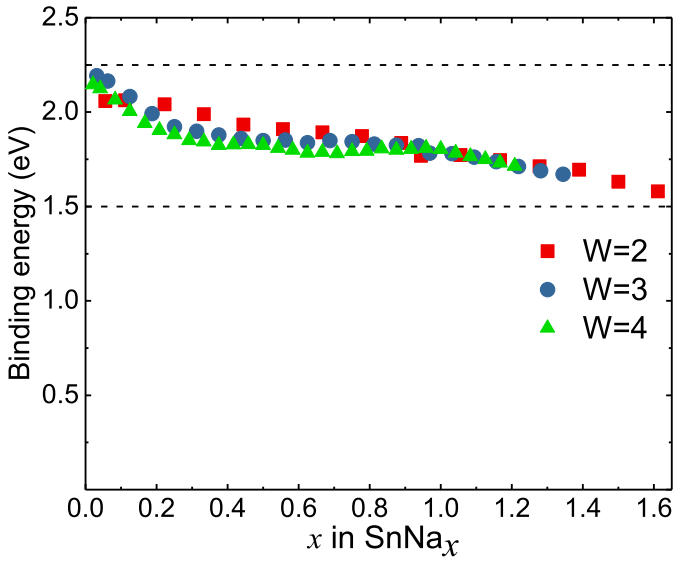

Fig. 6 Binding energies as a function of Na concentration (x) in Na adsorbed SnNM with W=2, 3, and 4. The SnNM structures correspond to a nanohole density of $4.44\times10^{13}\,cm^{-2}$, $2.79\times10^{13}\,cm^{-2}$, and $1.97\times10^{13}\,cm^{-2}$, respectively.

nanoholes (V^{H}_{Sn6}) on stanene. Similar to the case of graphene nanomesh, the edge of the holes has zigzag shape, see Fig. 4. W is the width of the wall between the nearest-neighboring holes and defined as the number of zigzag stanene chains in the wall. Here we consider different width between two holes (W=2, 3, and 4), which corresponds to different density of nanoholes in the SnNM. Here, we defined the nanohole density of SnNM as the number of nanohole per unit area on the stanene plane. As a result, the corresponding nanohole density is $4.44\times10^{13}\,cm^{-2}$, $2.79\times10^{13}\,cm^{-2}$ and $1.97\times10^{13}\,cm^{-2}$, respectively. After relaxation, the size of the SnNM supercells is nearly unchangeable compared with the pristine stanene supercells, as in the case of V^{H}_{Sn6} with one single nanohole. However, their difference is that periodic holes will slightly affect the Sn-Sn buckling height and bond length of the edge Sn atoms, which is larger and smaller than that of pristine stanene, respectively. For the Sn atoms far away from the holes, these parameters are close to those of pristine stanene.

Next, we studied the possible Na adsorption sties on the SnNM. We modeled five possible adsorption sites: H, T, B, E, and C, as shown in Fig. 5a, similar to the case of V^{H}_{Sn6}. For all the SnNMs, the binding energies at various adsorption sites follow the order: E > H > B ≥ T > C, see Table 2. Interestingly, for SnNM with W=4, after relaxation, Na moves to E site from the C site, and similar Na movement also happens in the V^{H}_{Sn6}, mainly due to the increase of the width of neighboring holes. Na ions at E and H site have a larger binding energy, indicating that they tends to be adsorbed at these sites. For H site, there are two symmetrical positions, namely above and below hollow sites. For E site, there

is only one position locating in the middle plane of stanene, and there are six equivalent E sites in a unit cell.

We also explored maximum adsorption concentration of Na ions on the SnNM. By analyzing Na binding energy and symmetry of SnNM, we modeled one possible Na adsorption scenario as below: Na ions occupy six E sites firstly, then all the H sites and C site (for W=4, no C site), and B sites lastly. It is noted that in a prior study of pristine stanene, the B site was not considered, because the pristine stanene will undergo a deformation and lattice distortion if Na atoms occupied other sites except the H sites.[36] In this work, we considered B sites as the last adsorption sites because the E site is in the middle plane of stanene and there is sufficient space at B sites to adsorb Na ions to avoid the deformation and lattice distortion. By assigning Na ions at all these possible sites, we are able to get a maximum Na adsorption concentration, *i.e.*, $SnH_{0.33}Na_{1.61}$, $SnH_{0.1875}Na_{1.34}$ and $SnH_{0.125}Na_{1.21}$ for W=2, 3 and 4, respectively. They correspond to atomic formulas $Sn_{18}H_6Na_{29}$, $Sn_{32}H_6Na_{43}$ and $Sn_{48}H_6Na_{58}$. At W=2, the SnNM has the largest Na adsorption concentration, see its relaxed structure in Fig. 5(b).

The binding energies as a function of Na concentration are also calculated, as shown in Fig. 6. Our results show that the binding energy decreases as Na concentration increases, indicating that the absorption becomes less stable because of the enhanced repulsive interaction between adjacent Na ions. However, the SnNM still maintains a quite large value ranging from 1.58 to 2.19 eV, which is much larger than the cohesive energy of bulk Na metal of 1.25 eV/atom in our calculation (1.11 eV/atom in experiment[51]). This indicates that Na atoms prefer to be adsorbed on the SnNM instead of forming bulk Na metal even at a maximum Na concentration.

3.4 Open-Circuit Voltage and Theoretical Capacity

The open-circuit voltage profile is a crucial measure of the performance of an anode material. It can be estimated by measuring the voltage over a range of metal atoms coverage. The charge/discharge process of SnNM for Na batteries follow the common half-cell reaction *versus* Na/Na^+:

$$(x_2-x_1)Na^+ + (x_2-x_1)e^- + Na_{x_1}SnNM \leftrightarrow Na_{x_2}SnNM \qquad (3)$$

Considering the above reaction, we calculated the average voltage of Na_xSnNM in the concentration range of $x_1 \le x \le x_2$ using the following equation:[52]

$$V \approx \frac{E_{Na_{x_1}SnNM} - E_{Na_{x_2}SnNM} + (x_2-x_1)E_{Na}}{(x_2-x_1)e} \qquad (4)$$

where $E_{Na_{x_1}SnNM}$ and $E_{Na_{x_2}SnNM}$ are the energies of $Na_{x_1}SnNM$, $Na_{x_2}SnNM$ compounds at concentrations x_1 and x_2, and E_{Na} is the energy per atom of Na in the bcc crystal. A calculated positive average voltage (V) means that the Na ions prefer to be adsorbed on the anode, while a negative value means that Na ions prefer to form Na cluster. The calculated voltage profile V as Na concentration (x) is shown in Fig. 7a. It shows that the voltage remains positive during the whole range of coverage values, indicating that SnNM is suitable to be the anode materials for Na-ion battery. The calculated V ranges from 1.99 V to 1.29 V for W=2, from 1.99 V to 1.26 V for W=3, from 2.01 V to 1.23 V for W=4. The average V are 1.61, 1.63, and 1.70 V for W=2, 3, and 4, which is comparable to those of the commercial anode materials such as TiO_2 with an open circuit voltage of 1.5-1.8 V.[53] To further optimize the performance of SnNM-based NIBs, some future research efforts may include: i) to reduce the voltage of the SnNM anode via doping engineering and surface modifications; ii) to search for corresponding high-voltage cathodes.

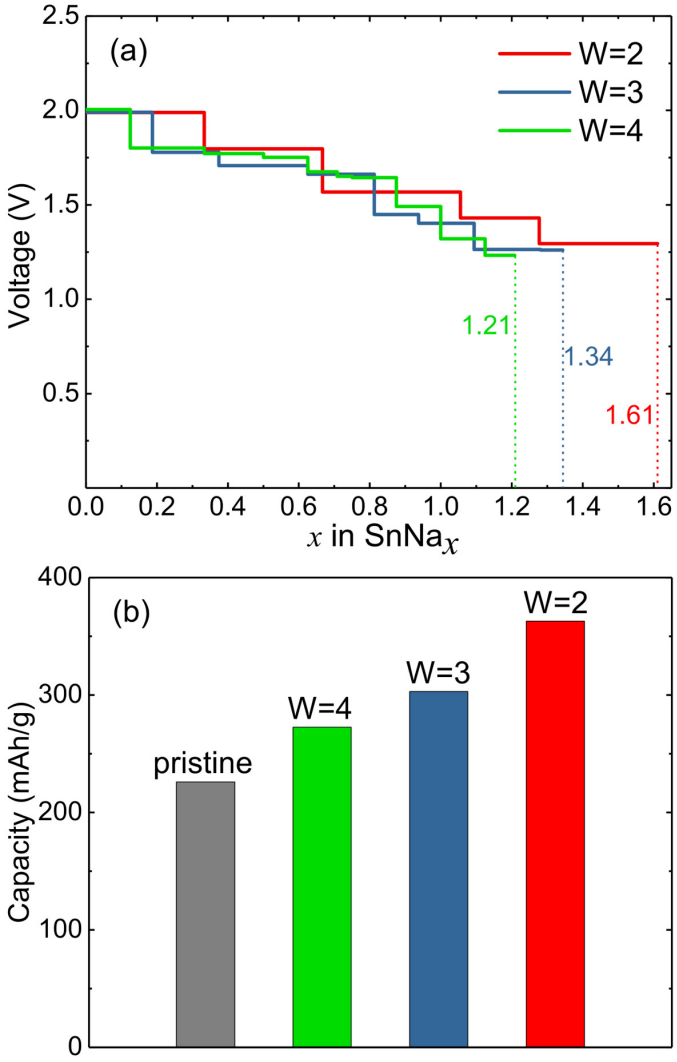

Fig. 7 Calculated voltage profiles and theoretical capacities. (a) Voltages as a function of Na concentration (x) in Na adsorbed SnNM with W=2, 3, and 4. (b) Theoretical capacities of pristine stanene and SnNM with W=2, 3, and 4.

We next calculated theoretical capacity C (mAh/g) at maximum Na concentration x using the formula,[7]

$$C = \frac{1}{M_{SnNM}}(x_{max} \times z \times F \times 10^3) \qquad (5)$$

where z is the valence number (z = 1 for Na), F is the Faraday constant (26.81 Ah/mol), and M_{SnNM} is the atomic mass of SnNM (119.05, 118.90, and 118.84 g/mol for W=2, 3, and 4,

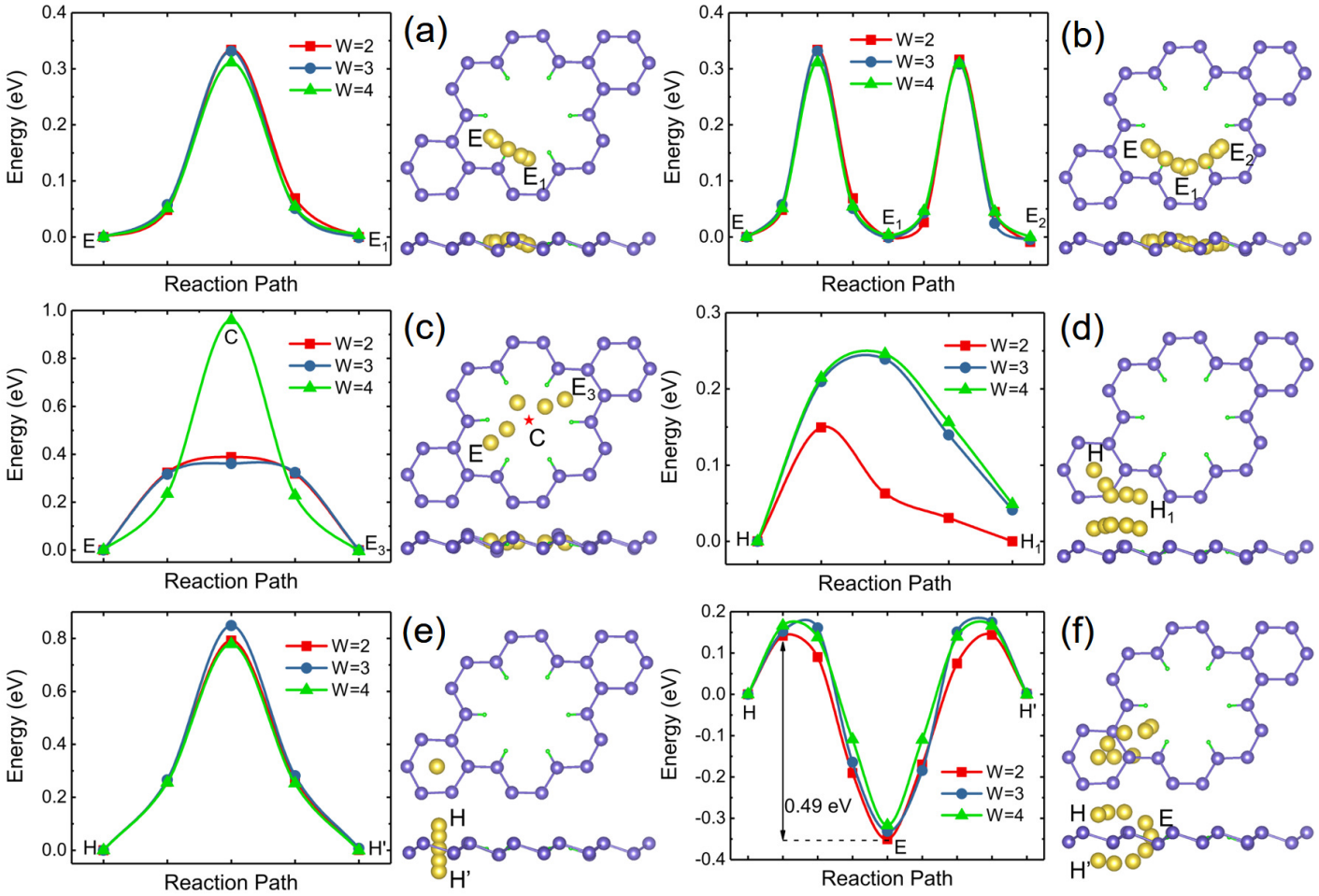

Fig. 8 Calculated Na diffusion barriers of SnNM with W=2, 3, and 4 along the six possible pathways: (a)E-E_1, (b)E-E_2, (c)E-E_3, (d)H-H_1, (e)H-H', and (f)H-E-H'. The corresponding top and side views of the optimized diffusion pathways in SnNM (W=2) are shown in the right panel for each case.

respectively). For pristine stanene, by assuming that one Na can only be adsorbed at one H site (this corresponds to a maximum Na mole concentration of 1.0), our calculated capacity is 225.8 mAh/g, which agrees well with the previous calculated value of 226 mAh/g.[36] For the SnNM with W=2, 3, and 4, their maximum Na mole concentrations are 1.61, 1.34, and 1.21, and their capacities are about 362.8, 303.0 and 272.6 mAh/g, respectively. These values are much larger than that of the pristine stanene (225.8 mAh/g), see Fig. 7b, indicating that the nanomesh structure can significantly improve the capacity of stanene. Moreover, these values are also much higher than other commercial TiO_2 and Ti_3C_2 based anode materials.[54] In short, these properties such as suitable operating voltage and increased specific capacity, make SnNMs promising anode materials for NIBs.

3.5 Na Diffusion

The diffusion energy barrier of metal ions in the anode materials is a key factor determining the charge-discharge rate of a battery.[55] A lower diffusion barrier implies a faster diffusion mobility and a higher charge-discharge rate in NIBs. Here we calculated diffusion energy barriers along several possible diffusion pathways using CI-NEB method. The modeled six possible diffusion pathways are shown in Fig. 8, which can be divided into four in-plane diffusion pathways and two out-of-plane diffusion pathways. The in-plane diffusion pathways include three ones in the nanohole including E-E_1, E-E_2, and E-E_3, as shown in Fig. 8(a-c), and one out the nanohole, H-H_1, as shown in Fig. 8d. The out-of-plane diffusion pathways are H-H' and H-E-H' as shown in Fig. 8(e-f). Our calculations reveal the following conclusions:

i) For in-plane diffusion, the diffusion energy barrier follows the order: H-H_1 < E-E_1 ≤ E-E_2 < E-E_3. Among all these four in-plane diffusion pathways, H-H_1 has the smallest diffusion energy barrier about 0.15 eV for SnNM with W=2, and 0.25 eV for W=3 and 4, see Fig. 8(d). These values are comparable to the energy barrier 0.16 eV on silicene,[14] 0.19 eV on $Na_2Ti_3O_7$,[56] and 0.28 eV on MoS_2.[10] These results indicate that the SnNM electrode has a comparable charge-discharge rate with these electrodes. The other two pathways E-E_1 and E-E_2 have the same energy barriers about 0.31∼0.33 eV because the pathway E-E_2 can be considered as the combination of E-E_1 and E_1-E_2 (equivalent to E-E_1), see Fig. 8a and 8b. For the pathway E-E_3, the calculated barrier is about 0.36 eV for W=2 and 3, and 0.96 eV for W=4, much larger than the other pathways, indicating that Na ions are unlikely to diffuse

along E-E_3 at lower density of nanoholes. In short, H-H_1 and E-E_1 can be assumed as the major in-plane diffusion pathways.

ii) For out-of-plane diffusion H-H', the calculated diffusion energy barrier for the three considered structures (W=2, 3, and 4) is nearly comparable, about 0.78∼0.85 eV, see Fig. 8e. This indicates that Na ions are not likely to move directly from H site above the stanene plane to the H' site below the stanene plane. For the pathway H-E-H', its diffusion barrier is about 0.48∼0.49 eV, decreased by about 40% compared to that of H-H', indicating that Na ions tend to penetrate stanene through the nanoholes. However, the out-of-plane diffusion barriers are generally larger than the in-plane diffusion barriers, thus implying that Na ions tends to move laterally along the stanene layer.

iii) The diffusion barrier not only depends on the diffusion pathway, but also relates to the nanohole density of SnNM. This point can be observed in the pathway E-E_3 and H-H_1, as shown in Fig. 8(c-d). For E-E_3, the diffusion barrier is 0.36∼0.39 eV for denser SnNMs (W=2 and 3), and 0.96 eV for less dense SnNM (W=4). The significant difference of the diffusion energy barrier is caused by the different pathway. For SnNM with W=2 and W=3, the optimized pathways can bypass the C site, while for SnNM with W=4, the pathway will go through the C site. For H-H_1, denser SnNM with W=2 has a much smaller diffusion barrier, 0.15 eV. For the other four diffusion pathways, SnNMs have similar diffusion energy barriers for all three considered SnNM. Therefore, the nanohole density mainly has an influence on the diffusion pathway H-H_1 that is also one of the dominant pathways. In other words, a denser nanomesh structure can lower the energy barrier and thus enable higher performance of NIBs.

In short, our calculations suggest that the major Na diffusion pathways include in-plane diffusion E-E_1 and H-H_1 and the out-of-plane diffusion H-E-H'. By combining these pathways, Na could diffuse along the whole surface of SnNM with a low diffusion energy barrier. Moreover, the calculated diffusion energy barriers are much smaller than those in the commercial anode materials such as TiO_2 with a barrier of 0.35∼0.65 eV[57] and bulk silicon with a barrier around 0.57 eV[58]. All these results suggest that SnNM can be a promising candidate electrode for NIBs. In addition, it is noted many 2D materials may undergo severe surface decomposition again the electrolyte during electrochemical cycling. Accordingly, materials stability of the SnNM again the electrolyte waits to be tested in the experiments.[59]

4 Conclusion

In summary, we have explored the possibility of using 2D stanene and nanohole-patterned SnNM as anode materials for NIBs using first-principles calculations. It is found that a nanohole defect consisting of six Sn vacancies in a hexagonal ring is energetically more favorable than other defects with less than six Sn vacancies, and moreover, the hydrogen passivation of the nanohole can further stabilize the nanohole defect. Our calculations show that nanohole defects in the stanene can significantly enhance Na binding intensity and lower Na diffusion barrier to as low as 0.15 eV with respect to Na adsorption on pristine stanene. A dense SnNM with high nanohole density can lead to a large Na adsorption concentration, theoretical capacity, and lower diffusion barrier. This works provides a proof of concept that a nanomesh structure is beneficial to enhance the performance of metal-ion battery in which the two-dimensional material serves as an electrode.

Conflicts of interest

There are no conflicts to declare.

Acknowledgment

This work was supported by the National Natural Science Foundation (No. 61675032, 61671085), the National Basic Research Program of China (973 Program) under Grant No. 2014CB643900, the BUPT Excellent Ph.D. Students Foundation (CX2017303), the Open Program of State Key Laboratory of Functional Materials for Informatics, the National Natural Science Foundation for Theoretical Physics special fund "cooperation program" (No. 11547039), and the Shaanxi Institute of Scientific Research Plan projects (No. SLGKYQD2-05). KY thanks Dr. Zheng Chen and Dr. Weiyang Li for useful discussions, and the financial support from the National Science Foundation under award number ACI-1550404.

References

1 J. M. Tarascon, *Nat. Chem.*, 2010, **2**, 510–510.
2 M. D. Slater, D. Kim, E. Lee and C. S. Johnson, *Adv. Fun. Mater.*, 2013, **23**, 947–958.
3 H. Pan, Y. Hu and L. Chen, *Energy Environ. Sci.*, 2013, **6**, 2338–2360.
4 V. Chevrier and G. Ceder, *J. Electrochem. Soc.*, 2011, **158**, A1011–A1014.
5 R. Alcántara, J. M. Jiménez-Mateos, P. Lavela and J. L. Tirado, *Electrochem. Commun.*, 2001, **3**, 639–642.
6 D. Stevens and J. Dahn, *J. Electrochem. Soc.*, 2001, **148**, A803–A811.
7 D. Er, J. Li, M. Naguib, Y. Gogotsi and V. B. Shenoy, *ACS Appl. Mater. Interfaces*, 2014, **6**, 11173–11179.
8 D. Çakır, C. Sevik, O. Gülseren and F. M. Peeters, *J. Mater. Chem. B*, 2016, **4**, 6029–6035.
9 B. Mortazavi, O. Rahaman, S. Ahzi and T. Rabczuk, *Appl. Mater. Today*, 2017, **8**, 60–67.
10 M. Mortazavi, C. Wang, J. Deng, V. B. Shenoy and N. V. Medhekar, *J. Power Source*, 2014, **268**, 279–286.
11 V. V. Kulish, O. I. Malyi, C. Persson and P. Wu, *Phys. Chem. Chem. Phys.*, 2015, **17**, 13921–13928.
12 H. Jiang, T. Zhao, Y. Ren, R. Zhang and M. Wu, *Sci. Bull.*, 2017, **62**, 572–578.
13 J. Hu, B. Xu, S. A. Yang, S. Guan, C. Ouyang and Y. Yao, *ACS Appl. Mater. Interfaces*, 2015, **7**, 24016–24022.
14 J. Zhu and U. Schwingenschlögl, *2D Mater.*, 2016, **3**, 035012.
15 H. I. Rasool, C. Ophus and A. Zettl, *Adv. Mater.*, 2015, **27**, 5771–5777.
16 J. Bai, X. Zhong, S. Jiang, Y. Huang and X. Duan, *Nat. Nanotechnol.*, 2010, **5**, 190–194.
17 A. Sinitskii and J. M. Tour, *J. Am. Chem. Soc.*, 2010, **132**,

14730–14732.
18 X. Liang, Y. S. Jung, S. Wu, A. Ismach, D. L. Olynick, S. Cabrini and J. Bokor, *Nano Lett.*, 2010, **10**, 2454–2460.
19 R. K. Paul, S. Badhulika, N. M. Saucedo and A. Mulchandani, *Anal. Chem.*, 2012, **84**, 8171–8178.
20 A. Esfandiar, N. J. Kybert, E. N. Dattoli, G. Hee Han, M. B. Lerner, O. Akhavan, A. Irajizad and A. Charlie Johnson, *Appl. Phys. Lett.*, 2013, **103**, 183110.
21 G. Ning, C. Xu, L. Mu, G. Chen, G. Wang, J. Gao, Z. Fan, W. Qian and F. Wei, *Chem. Commun.*, 2012, **48**, 6815–6817.
22 J. Yan, Z. Fan, W. Sun, G. Ning, T. Wei, Q. Zhang, R. Zhang, L. Zhi and F. Wei, *Adv. Fun. Mater.*, 2012, **22**, 2632–2641.
23 X. Zhu, X. Song, X. Ma and G. Ning, *ACS Appl. Mater. Interfaces*, 2014, **6**, 7189–7197.
24 Z. Fan, J. Yan, G. Ning, T. Wei, L. Zhi and F. Wei, *Carbon*, 2013, **60**, 558–561.
25 C. E. Ren, M.-Q. Zhao, T. Makaryan, J. Halim, M. Boota, S. Kota, B. Anasori, M. W. Barsoum and Y. Gogotsi, *ChemElectroChem*, 2016, **3**, 689–693.
26 Y. Xu, B. Yan, H. Zhang, J. Wang, G. Xu, P. Tang, W. Duan and S. C. Zhang, *Phys. Rev. Lett.*, 2013, **111**, 136804.
27 Y. Xu, Z. Gan and S. C. Zhang, *Phys. Rev. Lett.*, 2014, **112**, 226801.
28 J. Wang, Y. Xu and S. C. Zhang, *Phys. Rev. B*, 2014, **90**, 054503.
29 M. Liao, Y. Zang, Z. Guan, H. Li, Y. Gong, K. Zhu, X. Hu, D. Zhang, Y. Xu, Y. Wang *et al.*, *Nat. Phys.*, 2018, **1**,.
30 S. C. Wu, G. Shan and B. Yan, *Phys. Rev. Lett.*, 2014, **113**, 256401.
31 S. Saxena, R. P. Chaudhary and S. Shukla, *Sci. Rep.*, 2016, **6**, 31073.
32 F. Zhu, W. Chen, Y. Xu, C. Gao, D. Guan, C. Liu, D. Qian, S. C. Zhang and J. Jia, *Nat. Mater.*, 2015, **14**, 1020–1025.
33 P. Lu, L. Wu, C. Yang, D. Liang, R. Quhe, P. Guan and S. Wang, *Sci. Rep.*, 2017, **7**, 3912.
34 Z. Shi and C. V. Singh, *Nanoscale*, 2017, **9**, 7055–7062.
35 L. Wu, P. Lu, J. Bi, C. Yang, Y. Song, P. Guan and S. Wang, *Nanoscale Res. Lett.*, 2016, **11**, 525.
36 B. Mortazavi, A. Dianat, G. Cuniberti and T. Rabczuk, *Electrochimica Acta*, 2016, **213**, 865–870.
37 P. R. Abel, M. G. Fields, A. Heller and C. B. Mullins, *ACS Appl. Mater. Interfaces*, 2014, **6**, 15860–15867.
38 G. Kresse and J. Furthmüller, *Phys. Rev. B*, 1996, **54**, 11169–11186.
39 G. Kresse and D. Joubert, *Phys. Rev. B*, 1999, **59**, 1758–1775.
40 J. P. Perdew, K. Burke and M. Ernzerhof, *Phys. Rev. Lett.*, 1996, **77**, 3865–3868.
41 H. J. Monkhorst and J. D. Pack, *Phys. Rev. B*, 1976, **13**, 5188–5192.
42 W. Tang, E. Sanville and G. Henkelman, *J. Phys.: Condens. Matter*, 2009, **21**, 084204.
43 G. Henkelman, B. P. Uberuaga and H. Jónsson, *J. Chem. Phys.*, 2000, **113**, 9901–9904.
44 K. Tibbetts, C. R. Miranda, Y. S. Meng and G. Ceder, *Chem. Mater.*, 2007, **19**, 5302–5308.
45 B. Peng, F. Cheng, Z. Tao and J. Chen, *J. Chem. Phys.*, 2010, **133**, 034701.
46 A. Hashimoto, K. Suenaga, A. Gloter, K. Urita and S. Iijima, *Nature*, 2004, **430**, 870–873.
47 J. Sivek, H. Sahin, B. Partoens and F. M. Peeters, *Phys. Rev. B*, 2013, **87**, 085444.
48 H. Yang, M. Chshiev, D. W. Boukhvalov, X. Waintal and S. Roche, *Phys. Rev. B*, 2011, **84**, 214404.
49 M. Ricco, D. Pontiroli, M. Mazzani, M. Choucair, J. A. Stride and O. V. Yazyev, *Nano Lett.*, 2011, **11**, 4919–4922.
50 M. Bieri, M. Treier, J. Cai, K. Aït-Mansour, P. Ruffieux, O. Gröning, P. Gröning, M. Kastler, R. Rieger, X. Feng *et al.*, *Chem. Commun.*, 2009, **0**, 6919–6921.
51 C. Kittel, P. McEuen and P. McEuen, *Introduction to Solid State Physics*, Wiley New York, 1996, vol. 8.
52 M. Aydinol, A. Kohan, G. Ceder, K. Cho and J. Joannopoulos, *Phys. Rev. B*, 1997, **56**, 1354.
53 M. V. Koudriachova, N. M. Harrison and S. W. de Leeuw, *Solid State Ionics*, 2002, **152**, 189–194.
54 Q. Tang, Z. Zhou and P. Shen, *J. Am. Chem. Soc.*, 2012, **134**, 16909–16916.
55 S. P. Ong, V. L. Chevrier, G. Hautier, A. Jain, C. Moore, S. Kim, X. Ma and G. Ceder, *Energy Environ. Sci.*, 2011, **4**, 3680–3688.
56 H. Pan, X. Lu, X. Yu, Y. Hu, H. Li, X. Yang and L. Chen, *Adv. Energy Mater.*, 2013, **3**, 1186–1194.
57 C. L. Olson, J. Nelson and M. S. Islam, *J. Phys. Chem. B*, 2006, **110**, 9995–10001.
58 V. V. Kulish, O. I. Malyi, M. Ng, P. Wu and Z. Chen, *RSC Adv.*, 2013, **3**, 4231–4236.
59 Q. Bai, L. Yang, H. Chen and Y. Mo, *Adv. Energy Mater.*, 2018, 1702998.

Graphical Abstract

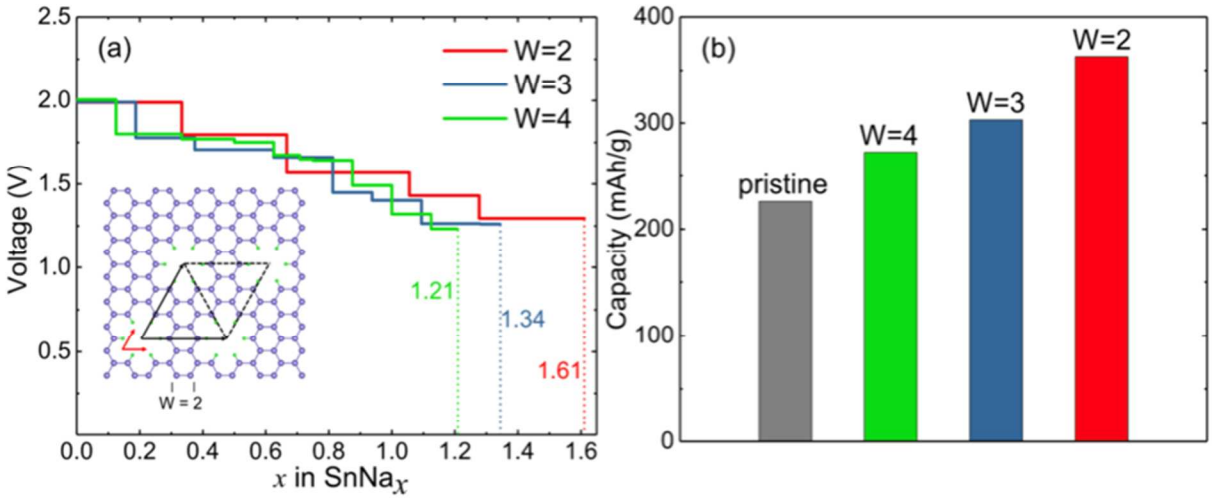

A two-dimensional stanene nanomesh is proposed as a promising anode material for Na-ion batteries.